LAWRENCE
LIVERMORE
NATIONAL
LABORATORY

UCRL-CONF-208083

Three-Dimensional Hydrodynamics Experiments on the National Ignition Facility

B. E. Blue

November 17, 2004

46th Annual Meeting of the Division of Plasma Physics
Savannah, GA, United States
November 15, 2004 through November 19, 2004

Disclaimer

UCRL-CONF-208083

Three-Dimensional Hydrodynamic Experiments on the National Ignition Facility

B. E. Blue,[1] S. V. Weber,[1] S. G. Glendinning,[1] N. E. Lanier,[2] D. T. Woods,[1] M. J. Bono,[1] S. N. Dixit,[1] C. A. Haynam,[1] J. P. Holder,[1] D. H. Kalantar,[1] B. J. MacGowan,[1] E. I. Moses,[1] A. J. Nikitin,[1] V. V. Rekow,[1] R. Wallace,[1] B. M. Van Wonterghem,[1] P. A. Rosen,[3] J. M. Foster,[3] P. E. Stry,[1] B. H. Wilde,[2] W. W. Hsing,[1] and H. F. Robey[1]

[1]Lawrence Livermore National Laboratory, Livermore, California 94550, USA

[2]Los Alamos National Laboratory, Los Alamos, New Mexico 87545, USA

[3]AWE Aldermaston, Reading, RG7 4PR, United Kingdom

(Dated: 7 February 2005)

ABSTRACT

The production of supersonic jets of material via the interaction of a strong shock wave with a spatially localized density perturbation is a common feature of inertial confinement fusion and astrophysics. The behavior of two-dimensional (2D) supersonic jets has previously been investigated in detail [J. M. Foster et. al, Phys. Plasmas 9, 2251 (2002)]. In three-dimensions (3D), however, there are new aspects to the behavior of supersonic jets in compressible media. In this paper, the commissioning activities on the National Ignition Facility (NIF) [J. A. Paisner *et al.*, Laser Focus World **30**, 75 (1994)] to enable hydrodynamic experiments will be presented as well as the results from the first series of hydrodynamic experiments. In these experiments, two of the first four beams of

NIF are used to drive a 40 Mbar shock wave into millimeter scale aluminum targets backed by 100 mg/cc carbon aerogel foam. The remaining beams are delayed in time and are used to provide a point-projection x-ray backlighter source for diagnosing the three-dimensional structure of the jet evolution resulting from a variety of 2D and 3D features. Comparisons between data and simulations using several codes will be presented.

I. Introduction

The interaction of a shock wave with a density perturbation is a problem of basic scientific interest [1] with specific application to astrophysics [2] and inertial confinement fusion (ICF) [3]. For instance, high Mach number hydrodynamic jets, which can result from a shock/perturbation interaction, are common features in astrophysics [4-7] and may result from the presence of capsule joints or cryogenic fill tubes in ICF [8]. Although the spatial scales of these systems vary over 16 orders of magnitude from supernova jets ($\sim 10^{10}$ m) to jets inside ICF capsules ($\sim 10^{-6}$m), they are unified by the physics of a high Mach number shock interacting with a perturbation at a two-fluid interface. In both systems the shock/perturbation interaction results in a jet of plasma being ejected ahead of the shocked material interface. In the case of supernovae, a jet provides a possible mechanism for explaining the observation of the early appearance of core high Z elements (nickel, iron, etc) [9] in the outer helium and hydrogen envelope. In the case of ICF capsules, fabrication joints or fill tubes can mix cooler shell material into the fuel before optimal compression, possibly affecting ignition [8]. To validate the simulations of these phenomena, there are several parameters of

critical importance. They are: the spatial dimensions, the characteristic velocities, the total mass of material, and the spatial mass distribution of the jet material. Previous work has studied 2D jet spatial evolution and their astrophysical scaling [6] and 2D and 3D jet's spatial and mass evolution [10]. In this paper, the commissioning activities on the National Ignition Facility (NIF) [11] to enable hydrodynamic experiments are presented as well as the results from the first series of hydrodynamic jet experiments. Comparisons between the experimental data and the radiation hydrocodes used to model them will be presented.

II. Experimental Setup

The experiments were conducted using the first quad (4 beams) of NIF [11] located at Lawrence Livermore National Laboratory. In this experiment, a 1.5 ns, 6 kJ (2x 3kJ beams), 3ω (351 nm wavelength), 1000 μm diameter laser pulse (intensity = 4×10^{14} W/cm^2) was used to drive a 40 Mbar shock wave into aluminum targets backed by 100 mg/cc carbon aerogel foam. The experimental package consisted of a 101±2 μm thickness aluminum disc placed in direct contact with a second aluminum disc of 149±2 μm thickness that contained a central, 162±2 μm diameter hole. The hole was drilled at either 0° for the case of a two-dimensional cylindrically symmetric target or 45° for the case of a fully three-dimensional target [Fig. 1(a)]. The two 800 μm diameter aluminum discs were inserted into a 2000 μm diameter, 250 μm thick gold washer that delayed the propagation of shocks around the exterior of the target package. The front surface of the target was coated with a 57±2 μm thick plastic (Parylene-N) ablator. The carbon aerogel

was encased in a polystyrene shock tube with a wall thickness of 40 μm.

The target package was diagnosed with pinhole-apertured point-projection radiography [12] as shown in Figure 1(b). An additional 2.5 kJ, 3ω, 1.5 ns, 500 μm diameter laser pulse (intensity = 6.7×10^{14} W/cm^2) illuminated the rear side of a 5 μm thick vanadium foil in order to create a 5.2 keV x-ray source. This backlighter laser pulse was delayed either 16 or 22 ns after the drive laser pulse so that the evolution of the target package could be imaged at two points in time. The 500 μm diameter x-ray source was apertured by a 20 μm diameter pinhole in a 50 μm thick, tantalum substrate to create a point source of x-rays. The point source was imaged through the experimental target onto a gated micro-channel plate (MCP) flexible x-ray imager (FXI) [13] with a magnification of 20. The MCP had a resolution of 60 μm [FWHM of the point spread function (14)] that corresponded to a target plane resolution of 3 μm. A 230 ps gate window was timed to capture a snapshot of the jet's hydrodynamic evolution with minimal motion blurring (~7 μm) while rejecting drive-laser generated x-rays that would increase the noise level of the image. Since the pinhole diameter was much greater than the FXI target plane resolution and the motion blurring, the overall target plane resolution was approximately equal to the pinhole diameter (20 μm). The FXI was filtered with 18 μm of aluminum that transmitted the 5.2 keV vanadium x-ray line while attenuating lower energy x-rays. An additional 125 μm of Kapton was used in the filter package to protect the FXI from debris.

Direct laser irradiation of the plastic ablator covering the planar aluminum surface results in a high-pressure shock that propagates into the Al disk. This shock heats the Al

to a temperature of approximately 20 eV, at which point it is in the plasma state. As the shock passes the interface between the two Al disks, plasma is ejected into the void in the second disk. This Al plasma then expands into the foam in the form of a supersonic jet. Figure 2 shows an experimental radiograph of a 3D target at t = 22 ns. In this radiograph, the gray scale used depicts the optically thick Al as a black or dark gray and the optically thin foam as a light gray color. The spatial scale of the resultant structure was calibrated to a reference grid on the target that consisted of 21 μm Au wires with a period of 63.5 μm. The contrast of the shock front exhibits some enhancement due to refraction [15]. Several key features of the jets observed in these experiments are highlighted in Fig. 2. They include: a pedestal of Al flowing down the shock tube behind the shock front, a compressed region of foam preceding the Al pedestal due to shock propagation on the foam itself, a jet of Al propagation ahead of the main shock in to the uncompressed foam, and an associated bow shock.

III. National Ignition Facility

NIF is a stadium-sized facility, which when completed will contain a 192-beam, 1.8-Megajoule, 500-Terawatt, ultraviolet laser system together with a 10-meter diameter target chamber with approximately 100 ports for diagnostic access to the experiment. NIF will be the world's largest and most energetic laser experimental system, providing a scientific center to study inertial confinement fusion and matter at extreme energy densities and pressures. In late 2002 NIF began activating its first four laser beam lines (known as a quad). By July 2003 NIF had delivered world-record single laser energy performance in primary (1.06 μm), second, and third harmonic wavelengths, and had

begun to perform experiments. In addition to the hydrodynamic experiments [10], other experiments studied laser-plasma interactions [16] and hohlraum dynamics.

In order to perform the present experiment on NIF, several capabilities had to be commissioned. These included the alignment of multiple targets, precision alignment and timing of beams, and beam spatial profile and temporal pulse shape conditioning. These will be separately described as follows. Figure 3(a) shows the measured spatial profile of a single drive beam (insert) in which the color scale represents intensity. Also plotted are a vertical lineout taken through the center of the profile (blue line) and a super-gaussian fit to the profile (red line). The profile had localized spots with intensity modulations of ±10% of the mean. The super-gaussian fit is $I = I_0 \exp\left(-2r / 1.08mm\right)^4$.

A new laser pointing fiducial technique was developed in which thin (33 μm) gold wires were attached to the driven face of the target. The tips of the gold wires were positioned outside the radial region of interest (r = 400 μm), but they were still illuminated by the edge of the laser spot. A static x-ray image of the drive face simultaneously recorded the relative positions of the laser and target. Figure 3(b) shows the result of this pointing measurement on 17 different shots. The data are shown as blue diamonds and the error bars were determined by the spatial resolution of the imaging detector. A mean pointing error of 51 μm with respect to the target was measured over the campaign.

Figure 4(a) shows the temporal pulse shape of the drive laser pulse. The measured temporal profile is shown in blue, while the nominally requested 1.5 ns flat top pulse is shown as a dotted red line. The drive pulse had a 1.2 ns, 2 TW flat top profile (90%-90%) with rise and fall times (10%-90%) of 275 ps and 440 ps, respectively. In

order to insure that repeatable data could be measured, shot-to-shot fluctuations in the drive laser energy needed to be kept below a threshold. Figure 4(b) shows the drive laser energy for both drive beams (blue and red points) as a function of shot number. The black line is the deviation from 6 kJ total drive energy. Deviations of up to 4% were observed from one shot to another. Since the velocity of the jet is proportional to the cube root of the laser energy [3], a 4% deviation in laser energy corresponds to a 1.6% velocity fluctuation. At 22 ns (the longest time delay in our experiment), a jet traveling at ~35 km/sec will have a positional variation of 12 μm due to the laser fluctuations. This is smaller than our 20 μm experimental resolution and thus it does not affect our experiment. It should be noted that since our experiment was insensitive to laser energy fluctuations, minimal effort was made to maintain a stable laser energy over our campaign. Nevertheless, the 2% rms variation of the laser energy was significantly less than the 8% rms functionality requirement for NIF.

IV. Hydrocode Simulations

A. Overview of the Codes

Four hydrocodes were used to simulate this experiment. They were Lasnex, Nym-Petra, Rage, Cale, and Hydra. Lasnex [17] is a two-dimensional rad-hydro code with a variety of options for Lagrangian or semi-Eulerian hydrodynamics and detailed modeling of all the ICF physics that can be resolved at the hydrodynamic length scales. This includes various options for laser-matter interaction, atomic physics, and coupling of the matter with the x-ray radiation.

The 2D experiment was also modeled using the AWE hydrocodes NYM [18] and PETRA [19,20]. NYM is a 2D Lagrangian hydrocode that includes laser ray trace and laser deposition packages, and non-local-thermodynamic equilibrium (NLTE) physics. The laser light is input as a 1-mm diameter spot on the axis of the calculation and its absorption is modeled as inverse bremsstrahlung in the coronal plasma. Radiation transport is treated by Monte Carlo photonics [21]. The NYM calculation proceeds until approximately 2 ns after the beginning of the laser pulse. After this time, the calculational timestep becomes impracticably small, and the simulation is transferred to the 2D Eulerian hydrocode PETRA. Radiation transfer is treated by single-group (gray) diffusion. Ion, electron and radiation temperatures are assumed equal (1-T model). Square, 5 um zones are used throughout the Eulerian mesh.

RAGE [22] (Radiation Adaptive Grid Eulerian) is a multidimensional, multimaterial Eulerian radiation-hydrodynamics code developed by Los Alamos National Laboratory and Science Applications International (SAIC). RAGE uses a continuous (in time and space) adaptive-mesh-refinement (CAMR) algorithm to follow interfaces and shocks, and gradients of physical quantities such as material densities and temperatures. RAGE uses a second-order-accurate Godunov hydrodynamics scheme similar to the Eulerian scheme of Colella [23]. Radiation transport is approximated with implicit gray flux-limited diffusion. The code has been validated with analytical test problems and many shock-tube, laser and pulsed-power experiments.

CALE [24] is a C-based arbitrary Lagrange Euler (ALE) 2D radiation hydrodynamics code. It uses a finite-differencing method to numerically solve the Euler equations. Equation-of-state data was input in tabular form. As an ALE code, it mixes

elements of Eulerian and Lagrangian techniques in order to inhibit mesh entanglement. HYDRA is a 3D ALE radiation hydrocode [25]. The simulation consisted of a 410 x 293 x 147 mesh covering a simulation region of 2.0 mm x 2.0 mm x 2.5 mm with grid sizes as small as 4 μm. The simulation is ALE, but relaxation kept the mesh in the jet approximately Cartesian. The measured 3D spatial intensity profile of the laser was included to more accurately model the experiment. Radiation transport was modeled in the gray diffusion approximation and the equations-of-state were generated off-line and input in tabular form.

In all five codes, the simulation was post-processed to produce a synthetic radiograph for comparison with the experimental data. Synthetic radiographs were generated from simulation data with post processing software that computed the absorption of backlighter photons through the simulation geometry along a specified line of sight. The backlighter source was approximated as a single 5.2 keV vanadium x-ray line and cold opacities of the target materials were used. Refraction [15], which enhanced edge definition in the experimental data, was not included in the synthetic radiographs. The synthetic radiographs were not blurred, to account for the 20 μm experimental resolution, to permit direct code-to-code comparison.

B. Results

To insure that the experiment was a valid platform to benchmark the codes, repeatable data was required. Figure 5(a) shows a side-by-side comparison of two separate 2D jet experimental radiographs in which repeatable data was acquired. Figure

5 also shows the comparison between simulated radiographs (right) and experimental data (left) of a 2D jet at 22 ns. Figures 5(b-f) are Lasnex, Cale, Nym-Petra, Rage, and Hydra, respectively. All five codes agree reasonably well on large-scale features of the jets. These include the height of the jet, the width of the jet's head, and the diameter of the stem. One large-scale disagreement between the codes is on the bow shock standoff distance. This is related to the compressibility of the low-density carbon foam and the different equations-of-state used. While accurately modeling the large-scale features of the jets, the four codes disagreed on the small-scale features. One example of this disagreement is in the shape of the head. The Nym-Petra simulation has a convex head, while the other three have concave heads of varying degree. An additional disagreement is found with the degree of roll up at the tip of the jet's head.

Even though the 2D jets were nominally cylindrically symmetric, non-uniformities in the drive laser spatial profile broke the symmetry. This necessitated the use of a fully three-dimensional code with a 3D laser deposition capability. Hydra was updated with the capability to include the measured 3D laser profile and to point the laser onto the target face. Figure 6 shows the comparison between the Hydra simulation and the data at 16 and 22 ns. Very good agreement is found between the two at both times. Not only are the large-scale features reproduced, but the data are suggestive of small-scale feature agreement as well. Specific examples are the shape of the stems, the shape of the heads, and the roll up at the tips of the jet. The experiment was able to capture high quality data in order to accurately measure the large-scale jet features. However, the 20-μm resolution and the limits on measuring low-optical depth regions (i.e. the roll up at

the tips of the jet) due to the background noise levels of the FXI, limited the ability of the experimental data to validate the small-scale flow features seen in the simulations.

Figure 7 shows the comparison between the 3D data (a), Hydra simulation (b), and Rage simulation (c) after 22 ns of evolution. As in the 2D case, good qualitative agreement is found between the large-scale features of the jet and the simulations. However, all three differ with respect to the small-scale features. Differences in the small-scale flow patterns are more pronounced between the simulations and the data in the 3D jet than the 2D one even when the 3D laser profile was included. This is expected since the Reynolds numbers of the experimental jets are very large ($\sim 10^7$ which is in the strongly turbulent regime), while the effective numerical Reynolds numbers of the simulations are orders of magnitude lower (limited by computational power). Therefore, the simulations do not accurately model the experiment with regards to the small-scale details. The differences between the 3D jets and the 2D jets are consistent with the observation that the 3D flow has a fully three-dimensional vorticity field, whereas in the 2D case, the vorticity is non-zero only in the azimuthal component. The 3D jets can transition to a turbulent state faster since the 2D jets need time for instabilities to break symmetry and seed the three-dimensional vorticity field characteristic of a turbulent flow.

In addition to the spatial scales of the jet, the amount of material in a jet is a quantity of critical importance. The mass calculation used conservation of mass to account for the mass of shocked foam preceding the Al pedestal. The difference in transmitted intensity in a region ahead of the shock will be related to the total mass of Al and foam pushed up by the pedestal. Regardless of symmetry, the total Al mass is given by:

$$m_{Al} = \frac{-1}{\mu_{Al}} \left(\int_S \ln\left(\frac{I}{I_0}\right) dS + \mu_f m_f \right)$$

Here m_{Al}, m_f, μ_{Al}, μ_f, S, I, and I_0 are the measured Al mass, the mass of the foam displaced by the pedestal, the Al mass absorption coefficient (166.6 cm^2/g), the foam mass absorption coefficient (16.8 cm^2/g), the surface over which the mass is calculated, the transmitted intensity, and the transmitted intensity through the uncompressed foam respectively. This method results in a measurement of the total Al mass, since it removes the contribution of the compressed foam. The error in the mass is due to the FXI-induced noise and background levels of the data. This error was estimated to be ±0.5 μg. Figure 8 shows the mass of jet material extending beyond the pedestal/foam interface as a function of time for the cases of 2D [Fig. 8(a)] and 3D perturbations [Fig. 8(b)]. The experimental data points are depicted as black diamonds, Hydra simulations as solid red lines, Cale as a dashed black line, Nym-Petra as a solid blue line, and Lasnex as a dashed blue line. In the 2D jets, both Hydra and Lasnex predicted the mass to increase as a function of time, but Nym-Petra and Cale show a leveling off of total jet mass at the later times. This is due to the interplay between the progression of the jet and that of the pedestal. The observable jet mass is defined as the mass ahead of the pedestal, and at the later times in the Nym-Petra simulation, the non-planarity of the pedestal is obscuring part of the jet [Fig 5(d) inset]. This obscuration led to the decrease in observable jet mass. This was confirmed since the total jet mass (including the region obscured by the pedestal) in Nym-Petra was in agreement with the other codes. A similar obscuration by the pedestal is thought to account for the discrepancy between the simulation and the 3D jet data at the early time. At early times the 3D jet has a large percent of its mass near the

pedestal. Therefore, small deviations in the modeling or measurement of the jet ahead of the pedestal can lead to larger variations in the measured mass.

V. Future Hydro experiments on NIF

As NIF progresses towards completion, it will continue to improve as an experimental platform for hydrodynamic experiments. The current experiment was limited to the first quad of beams. This limited the amount of energy that was available, the maximum time delay, and the geometry of the experiment. As the facility evolves, more energy will be available to drive the experiment. This will permit larger, hotter, and faster jets that will allow a more thorough measurement of the jets small-scale flow features. While the first quad of beams limited the maximum time delay to 22 ns, the addition of more beams will allow for delays of 100s of ns or more. With the longer time delay, the transition to turbulence in the high Reynolds number jet flow can be systematically studied. Finally, as more beams are available for experiments, convergent geometry, as well as planer geometry, flows will be able to be studied.

VI. Conclusions

In these experiments, high quality, repeatable, 2D and 3D jet data were acquired. The jet data were used to benchmark a wide variety of 2D and 3D hydrocodes. Comparisons between the data and the simulations resulted in qualitative agreement of the large-scale features of the jets in all of the codes. One of these codes, Hydra, was

updated with an improved EOS for the foam and a 3D laser deposition capability. These improvements resulted in good qualitative agreement between Hydra and the data. These results aid our understanding of the complex hydrodynamics in supernovae and also of the physical processes relevant to ignition of NIF ICF capsules.

Acknowledgements

This work was performed under the auspices of the U. S. Department of Energy by Los Alamos National Laboratory under Contract No. W-7405-ENG-36 and by Lawrence Livermore National Laboratory under Contract No. W-7405-ENG-48.

References

[1] R. C. Davidson, D. Arnett, J. Dahlburg, P. Dimotakis, D. Dubin, G. Gabrielse, D. Hammer, T. Katsouleas, W. Kruer, R. Lovelace, D. Meyerhofer, B. Remington, R. Rosner, A. Sessler, P. Sprangle, A. Todd, J. Wurtele, Frontiers in High Energy Density Physics: The X-Games of Contemporary Science, (The National Academies Press, Washington, D.C., 2003).

[2] H. F. Robey, T. S. Perry, R. I. Klein, J. O. Kane, J. A. Greenough, and T. R. Boehly, Phys. Rev. Lett. **89**, 085001 (2002).

[3] J. D. Lindl, Phys. Plasmas **2**, 3933 (1995).

[4] B. Reipurth and J. Bally, Ann. Rev. Astron. and Astrophys. **39**, 403 (2001).

[5] V. Icke, G. Mellema, B. Balick, F. Eulderink, and A. Frank, Nature **355**, 524 (1992).

[6] J. M. Foster, B. H. Wilde, P. A. Rosen, T. S. Perry, M. Fell, M. J. Edwards, B. F. Lasinski, R. E. Turner, and M. L. Gittings, Phys. Plasmas **9**, 2251 (2002).

[7] A. M. Khokhlov, P. A. Höflich, E. S. Oran, J. C. Wheeler, L. Wang, and A. Yu. Chtchelkanova, Astrophys. J. Lett. **524**, L107 (1999).

[8] S. R. Goldman, S. E. Caldwell, M. D. Wilke *et al.*, Phys. Plasmas **6**, 3327 (1999).

[9] L. Wang, J. C. Wheeler, P. Höflich *et al.*, Astrophys. J. **579**, 671 (2002).

[10] B. E. Blue, S. V. Weber, S. G. Gelndinning *et al.*, Accepted for Publication in Phys. Rev. Lett. (2005).

[11] J. A. Paisner, J. D. Boyes, S. A. Kumpan, W. H. Lowdermilk, and M. Sorem, Laser Focus World **30**, 75 (1994).

[12] J. Workman, J. R. Fincke, P. Keiter *et al.*, Rev. Sci. Instrum. **75**, 3915 (2004).

[13] K. S. Budil, T. S. Perry, P. M. Bell, J. D. Hares, P. L. Miller, T. A. Peyser, R. Wallace, H. Louis, and D. E. Smith, Rev. Sci. Instrum. **67**, 485 (1996).

[14] H. F. Robey, K. S. Budil, and B. A. Remington, Rev. Sci. Instrum. **68**, 792 (1997).

[15] D. S. Montgomery, A. Nobile, and P. J. Walsh, Rev. Sci. Instrum. **75**, 3986 (2004).

[16] S.H. Glenzer, P. Arnold, G. Bardsley *et al.*, Nucl. Fusion **44**, S185 (2004).

[17] G. B. Zimmerman and W. L. Kruer, comments in *Plasma Physics and Controlled Fusion* 2, 51 (1975).

[18] P. D. Roberts, S. J. Rose, P. C. Thompson and R. J. Wright, J. Phys. D **13**, 1957 (1980).

[19] D. L. Youngs, in Numerical Methods for Fluid Mechanics, edited by K. W. Morton and M. J. Baines (Academic, London, 1982)

[20] D. L. Youngs, Physica D 12, 32 (1984).

[21] J. A. Fleck and J. D. Cummings, J. Comput Phys. **8**, 313 (1971).

[22] M. L. Gittings, in *Numerical Methods Symposium*, 28–30 April 1992. Copies may be ordered from Defence Nuclear Agency, 56801 Telegraph Road, Alexandria, VA 22310-3398.

[23] P. Colella, SIAM J. Sci. Statist. Comput. **6**, 104 (1985).

[24] R. T. Barton, Numerical Astrophysics (Jones and Bartlett, Boston, 1985).

[25] M. M. Marinak, R. E. Tipton, O. L. Landen *et al.,* Phys. Plasmas **3**, 2070 (1996).

Figure 1. An expanded view of the target package with each individual component labeled (a) and a schematic of the radiographic configuration (not to scale) used on NIF (b).

Figure 2. Experimental radiograph of a 3D target at 22 ns highlighting key jet features. The data was rotated so that the jet and shock direction are vertical. The positions of the pre-shocked Al plug, Al washer, and Au Washer are also outlined.

Figure 3. Laser spatial intensity profile (a) and the pointing accuracy of the drive laser beams on the target face (b). The profile had localized spots of intensity that had amplitudes of ±10%. The super-gaussian fit parameters were a fit of order four and a full-width half-maximum spot size of 1.08 mm. The laser had a mean pointing error of 51 μm.

Figure 4. Laser temporal profile for the drive beams (a). The measured temporal profile is shown in blue, while the nominally requested 1.5 ns square pulse is shown as a dotted red line. The energy stability of the drive laser over the three-week campaign is shown in (b). The energy of each of the drive beams (blue circles and red diamonds) was close to the requested 3 kJ. The deviation in total drive energy from the mean energy (black diamonds) was small (<4%) over the campaign.

Figure 5. Side by side comparisons of 22 ns 2D jet data. Repeatability was demonstrated by comparing two sets of data (a). Data (left) was compared against the simulations

(right) for Lasnex (b), Cale (c), Nym-Petra (d), Rage (e), and Hydra (f). Parameters used in the simulations were identical to those in the experiment. All four codes and the data agreed on the large-scale features of the jet, however, small-scale features differed amongst the codes. A density slice from the Nym-Petra simulation that was used to generate the synthetic radiograph is shown as an inset in (d).

Figure 6. Side by side comparison of data (left) and Hydra (right) at t = 16 ns (a) and t = 22 ns (b). Using the 3D laser intensity profile, Hydra achieved good agreement with the data in both the large and small-scale features.

Figure 7. Comparison of radiographs of 3D jets at 22 ns. Data is shown in (a), Hydra in (b), and Rage in (c). While the large-scale features of the simulations agree with the data, the discrepancy of the small-scale features is greater than in the 2D jet case. This is indicative that the 3D jets may be transitioning to a turbulent state.

Figure 8. Jet mass vs. time for both the 2D jet (a) and 3D jet (b). Experimental data is shown as black diamonds. The simulation results from Hydra, Cale, Lasnex, and Nym-Petra are shown as a solid red line, a dashed black line, a dashed blue line, and a solid blue line, respectively.

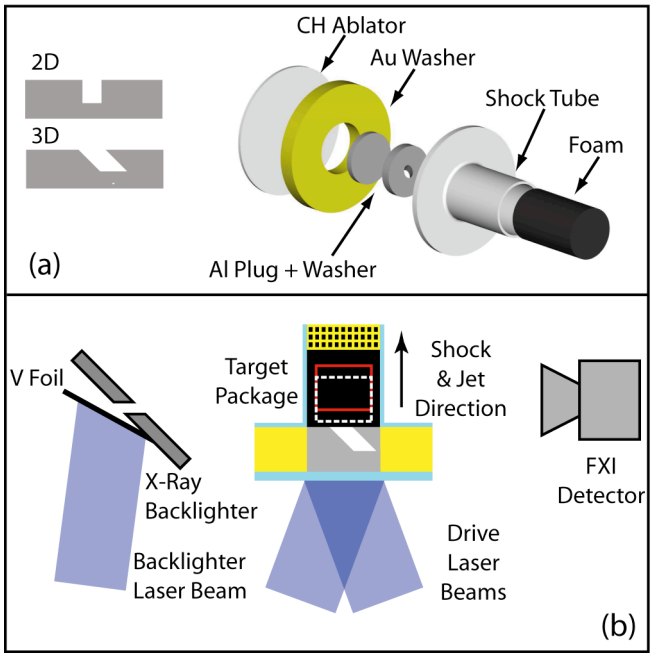
CH Ablator
Au Washer
2D
3D
Shock Tube
Foam
(a)
Al Plug + Washer
V Foil
Target
Package
Shock
& Jet
Direction
FXI
Detector
X-Ray
Backlighter
Drive
Laser
Beams
Backlighter
Laser Beam
(b)

Figure 1

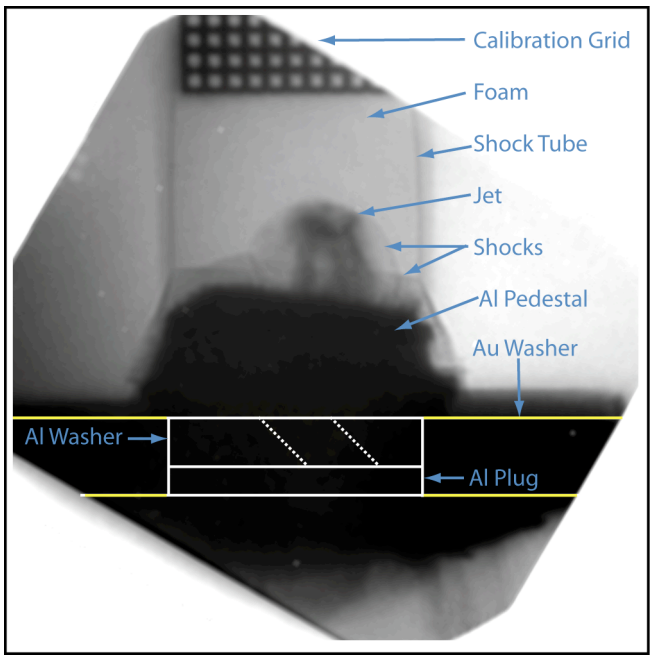
Calibration Grid
Foam
Shock Tube
Jet
Shocks
Al Pedestal
Au Washer
Al Washer
Al Plug

Figure 2.

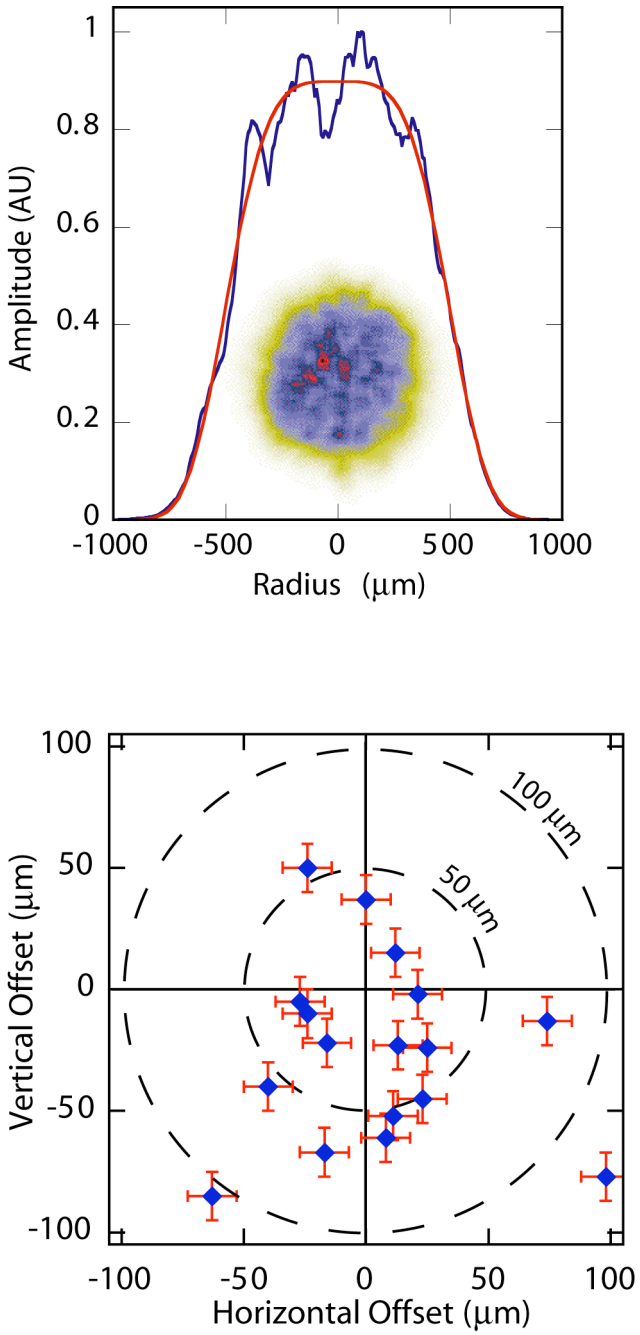
Amplitude (AU)
Radius (µm)
Vertical Offset (µm)
Horizontal Offset (µm)
100 µm
50 µm

Figure 3.

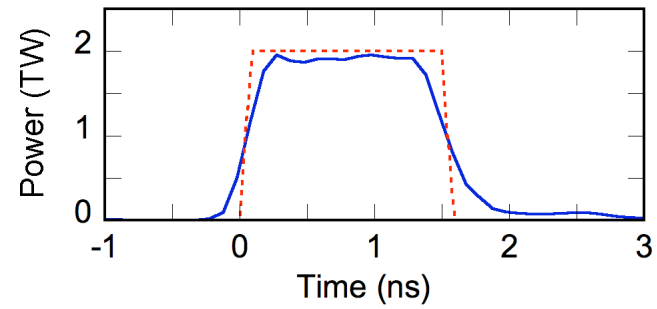
Power (TW)
2
1
0
-1
0
1
2
3
Time (ns)

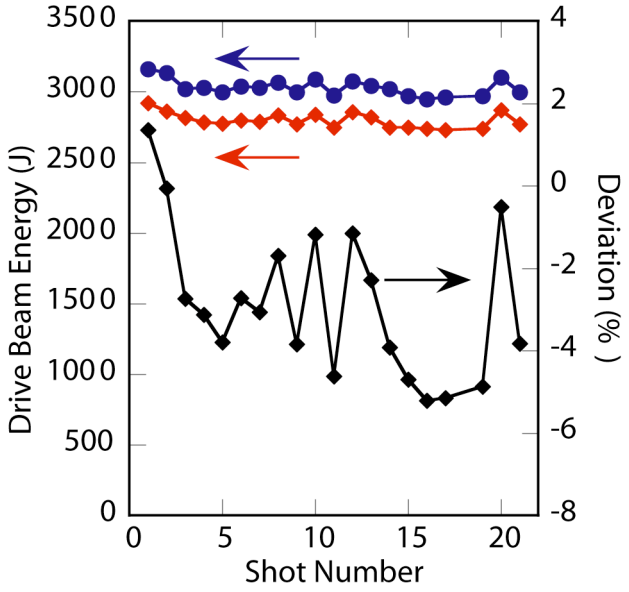
Drive Beam Energy (J)
3500
3000
2500
2000
1500
1000
500
0
4
2
0
-2
-4
-6
-8
Deviation (%)
0
5
10
15
20
Shot Number

Figure 4.

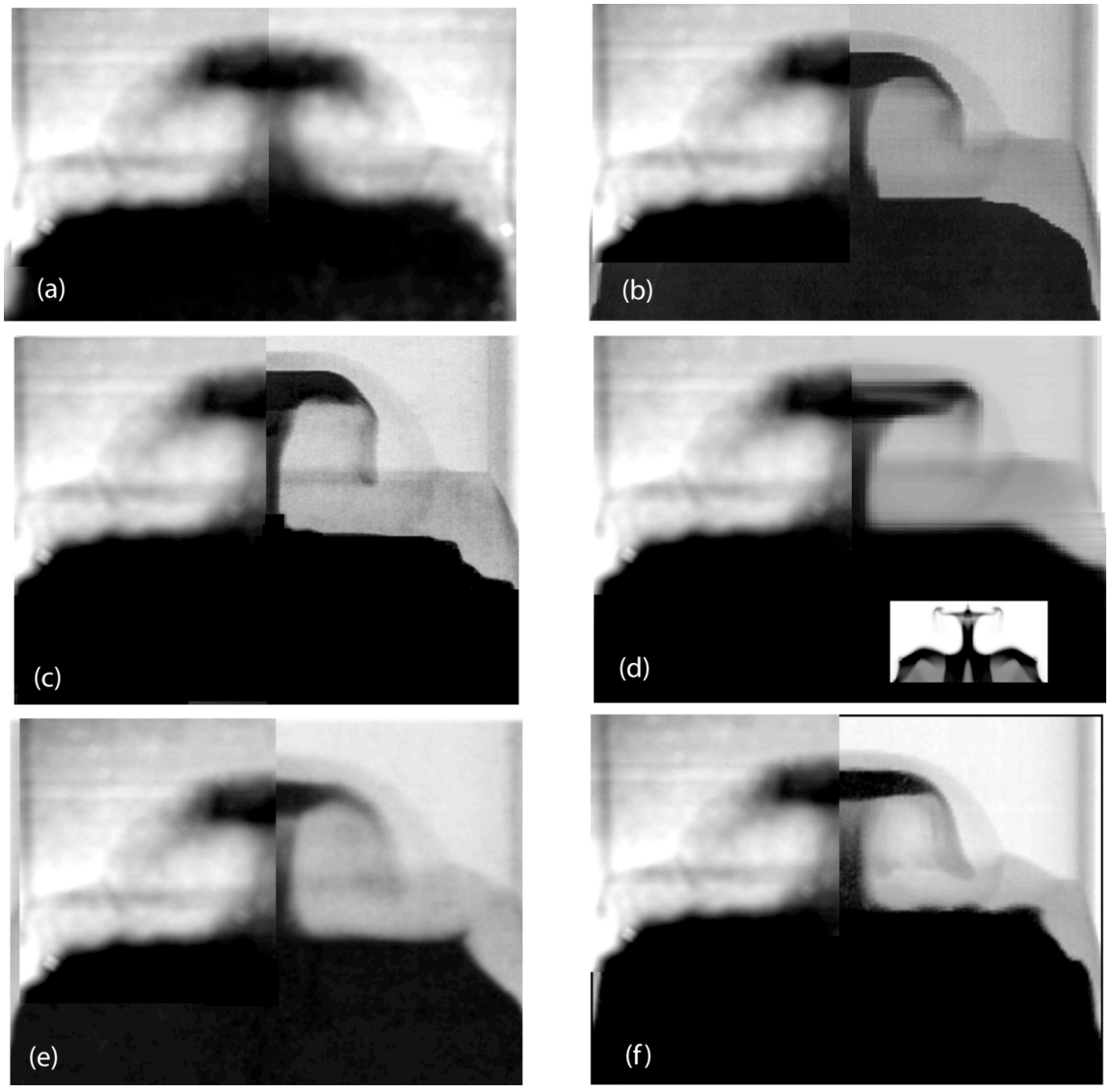

Figure 5.

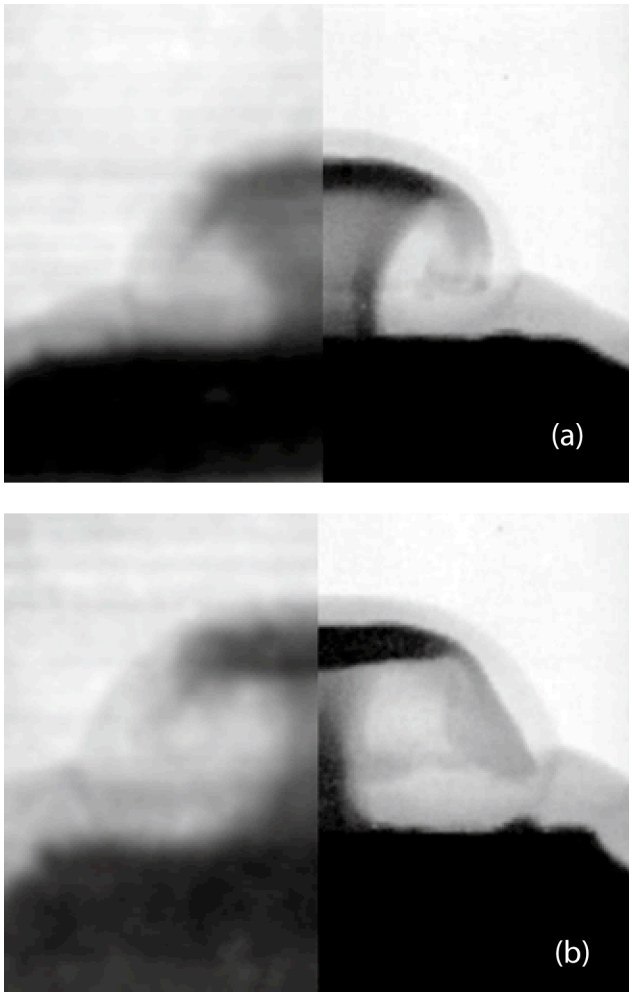

Figure 6.

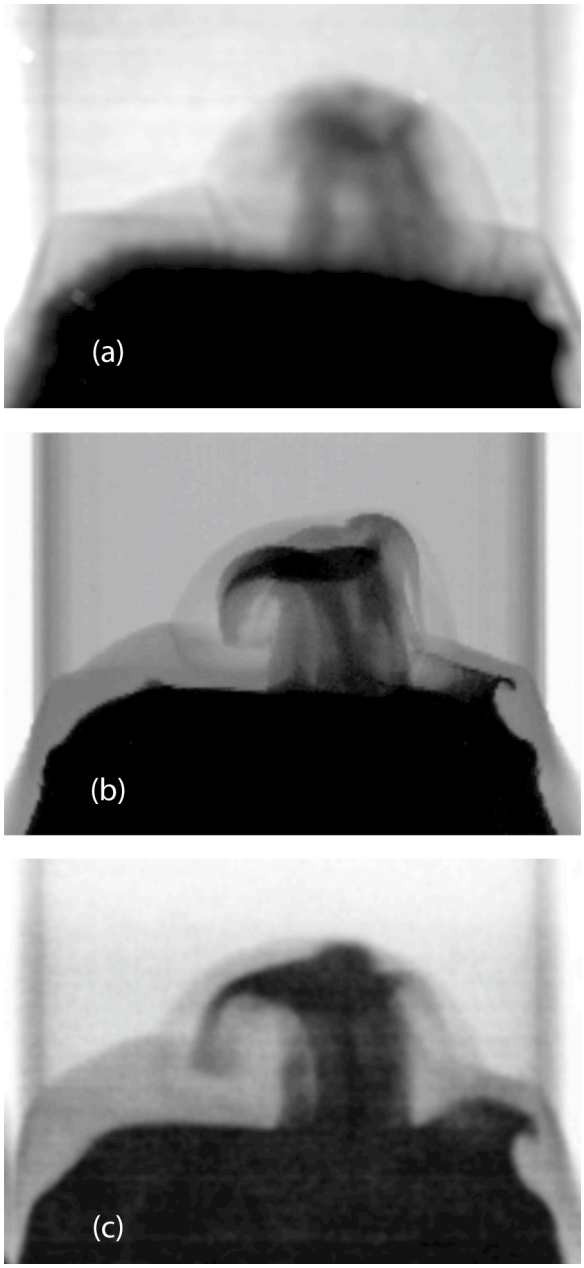

Figure 7.

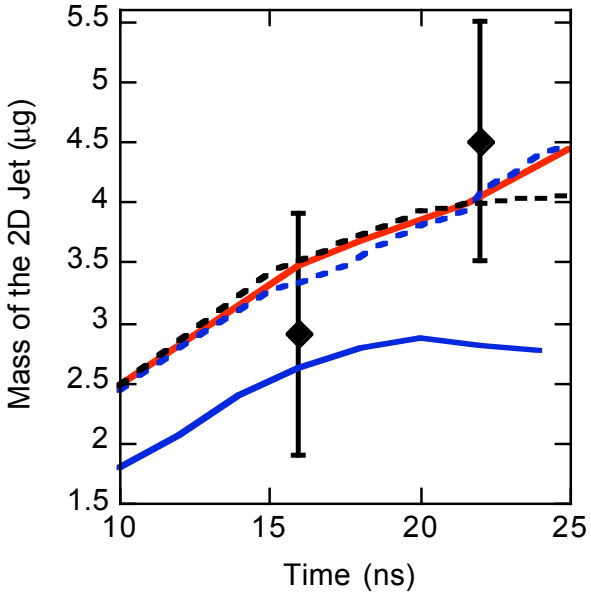
Mass of the 2D Jet (µg)
5.5
5
4.5
4
3.5
3
2.5
2
1.5
10
15
20
25
Time (ns)

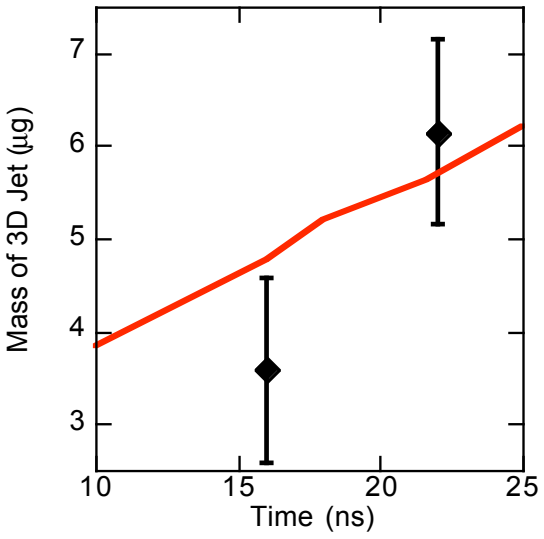
Mass of 3D Jet (µg)
7
6
5
4
3
10
15
20
25
Time (ns)

Figure 8.